

RESEARCH ARTICLE

10.1002/2015JD023718

Key Points:

- Satellite-supported WRF-UCM is developed using MODIS observed GVF and albedo
- Satellite observations are implemented over both urban and vegetated pixels
- Urban heat island in Los Angeles is related to surface characteristics

Supporting Information:

- Figures S1–S16

Correspondence to:

G. Ban-Weiss,
banweiss@usc.edu

Citation:

Vahmani, P., and G. A. Ban-Weiss (2016), Impact of remotely sensed albedo and vegetation fraction on simulation of urban climate in WRF-urban canopy model: A case study of the urban heat island in Los Angeles, *J. Geophys. Res. Atmos.*, 121, 1511–1531, doi:10.1002/2015JD023718.

Received 27 MAY 2015

Accepted 2 JAN 2016

Accepted article online 7 JAN 2016

Published online 19 FEB 2016

Impact of remotely sensed albedo and vegetation fraction on simulation of urban climate in WRF-urban canopy model: A case study of the urban heat island in Los Angeles

P. Vahmani¹ and G. A. Ban-Weiss¹

¹Department of Civil and Environmental Engineering, University of Southern California, Los Angeles, California, USA

Abstract Modeling the climate of urban areas is of interest for studying urban heat islands (UHIs). Reliable assessment of the primary causes of UHIs and the efficacy of various heat mitigation strategies requires accurate prediction of urban temperatures and realistic representation of land surface physical characteristics in models. In this study, we expand the capabilities of the Weather Research and Forecasting (WRF) model by implementing high-resolution, real-time satellite observations of green vegetation fraction (GVF) and albedo. Satellite-based GVF and albedo replace constant values that are assumed for urban pixels in the default version of WRF. Simulations of urban meteorology in Los Angeles using the improved model show marked improvements relative to the default model. The largest improvements are for nocturnal air temperatures, with a reduction in root-mean-square deviation between simulations and observations from 3.8 to 1.9°C. Utilizing the improved model, we quantify relationships between surface and 2 m air temperatures versus urban fraction, GVF, albedo, distance from the ocean, and elevation. Distance from the ocean is found to be the main contributor to variations in temperatures around Los Angeles. After conditionally sampling pixels to minimize the influence of distance from the ocean and elevation, we find that variations in GVF and urban fraction are responsible for up to 58 and 27% of the variance in temperatures. The satellite-supported meteorological modeling framework reported here can be used for studying UHIs in other cities and can serve as a foundation for testing the efficacy of various heat mitigation strategies.

1. Introduction

Urban areas cover a small fraction of Earth's surface. However, roughly 54% of the global population currently lives in urban areas, and this number is expected to reach 66% by 2050 [United Nations, 2014]. Urbanization impacts the exchange of energy, water, and momentum between the land surface and atmosphere at local to regional scales. This occurs through changes in land surface physical characteristics (henceforth referred to as "surface physical characteristics") such as albedo, emissivity, vegetation fraction, and roughness, which control land-atmosphere interactions.

Numerical modeling has been utilized to shed light on the relative importance of various surface physical characteristics in dictating land-atmosphere coupling [Wetzel and Chang, 1988; Molders, 2001; Vahmani and Hogue, 2014a]. Wetzel and Chang [1988] evaluated the significance of surface physical characteristics on simulating regional evapotranspiration (ET) using an ET model coupled with a one-dimensional atmospheric boundary layer model. They highlighted the importance of leaf area index (LAI), fractional green vegetation cover, and roughness length for accurately predicting ET. Uncertainty analysis conducted by Molders [2001] suggested that realistic representation of plant and soil parameters (i.e., albedo, evaporative conductivity, roughness length, soil volumetric heat capacity, field capacity, capillarity, and emissivity) should be prioritized in mesoscale modeling. Vahmani and Hogue [2014a] investigated the relative importance of surface physical characteristics for accurately predicting ET in the Noah land model coupled to an urban canopy model (Noah-UCM). They found that green vegetation fraction (GVF) plays the most significant role in reproducing observations of ET. These studies confirm that realistic domain-specific information on surface physical characteristics is critical for accurately modeling land-atmosphere interactions in numerical weather prediction models, over both urban and natural surfaces. However, most mesoscale modeling frameworks, such as the Weather Research and Forecasting (WRF) model, rely on either land cover-dependent lookup tables or outdated low-resolution climatological data sets to define these surface physical characteristics.

Further, the models assume constant values for some surface physical characteristics over urban areas and therefore do not take into account the high-resolution variability that can be found in these regions.

With a quasi-continuous and comprehensive mapping of Earth, satellite remote sensing is a unique data source for characterizing the land surface. These data have been used to derive model inputs that describe land surface characteristics for numerical weather and climate simulations [Crawford *et al.*, 2001; *de Foy et al.*, 2006; Meng *et al.*, 2009]. However, there are relatively few studies that apply satellite observations to describe urban surface characteristics in modeling urban climate. A few studies have employed satellite observations to update outdated maps of land cover type that are used by default as inputs to mesoscale models [Cheng and Byun, 2008; Cheng *et al.*, 2013; Li *et al.*, 2014]. When compared to observations, these studies reported improved model prediction of urban meteorology including boundary layer characteristics, wind patterns, and air temperatures. Other studies have utilized remotely sensed observations that represent morphological data over urban areas [Taha, 2008a, 2008b; Salamanca *et al.*, 2011]. These data sets improve representation of urban canopy parameters (e.g., building height, height-to-width ratio, urban fraction, and roughness length) in mesoscale models such as the urbanized meteorological model (uMMS) and WRF. Other studies have used remote sensing for deriving roof albedos for use in WRF [Ban-Weiss *et al.*, 2015a, 2015b]. Limited past research has taken advantage of satellite observations to directly improve representation of surface physical characteristics (as opposed to just land cover type) and associated parameters over highly heterogeneous and complex urban surfaces in mesoscale meteorological models [Vahmani and Hogue, 2014a; Li *et al.*, 2014]. Vahmani and Hogue [2014a] utilized fused Landsat-MODIS observations over a small region of Los Angeles to improve the representation of GVF, impervious surface area, albedo, LAI, and emissivity in the offline version of Noah-UCM. Simulated ET was nearer to ground observations after implementing the remotely sensed surface physical characteristics in the model. Li *et al.* [2014] attempted to improve WRF by implementing MODIS-based GVF and LAI as well as remotely sensed land cover maps for the Pearl River Delta region of China. Their simulations were nearer to observations, relative to the default model, when the satellite-derived land surface physical characteristics were used as inputs to WRF.

The urban heat island (UHI) is a phenomenon in which urban areas are hotter than rural surroundings [Manley, 1958], potentially resulting in human discomfort and increased building energy consumption [Lee and Park, 2008; Susca *et al.*, 2011; Loughner *et al.*, 2012]. Given that the UHI is one of the most prominent phenomena in urban climate [Oke, 1982; Arnfield, 2003], its accurate simulation by mesoscale models applied over urban areas is important. The UHI is generally understood as being caused by a shift in the surface energy partitioning toward lower latent heat flux and higher sensible heat flux. This is mainly attributed to the fact that in urban areas, vegetation and evaporating soil surfaces are replaced by impervious surfaces such as asphalt concrete with high heat storage capacity and often distinctly low albedo [Oke, 1982; Grimmond, 2007]. The UHI develops at the surface and through the lower atmosphere, from the urban canopy layer to the boundary layer, and can be assessed using land surface or air temperatures [Rao, 1972; Oke, 1976; Voogt and Oke, 2003]. The air temperature UHI is in many locations a nocturnal phenomenon [Oke, 1982], whereas the surface temperature UHI is usually greatest during the day [Roth *et al.*, 1989], and is more easily related to surface characteristics [Owen *et al.*, 1998; Voogt and Oke, 2003; Nichol and Wong, 2005]. Recent research has shown that the efficiency with which convective heat is transferred from the surface to the boundary layer also plays an important role in determining UHI intensity [Zhao *et al.*, 2014].

Assessment of the UHI requires accurately representing surface or near-surface air temperatures within and surrounding an urban region. The first goal of this study is to investigate the extent to which prediction of spatial and temporal variation in these temperatures can be improved in a mesoscale meteorological model (WRF-UCM) by enhancing the representation of land surface physical characteristics within and surrounding a city. This enhancement is implemented using high-resolution and real-time gridded MODIS-based observations to derive important land surface physical characteristics, including GVF and albedo. To enable the use of satellite-based GVF and albedo, the model was modified since the default version of WRF-UCM assumes predefined and unvarying GVF and albedo values for the pervious portion of urban grid cells. This change allows for including heterogeneity of real-time domain-specific GVF and albedo over urban areas. The role of these model enhancements in improving the simulation of urban heat islands is then assessed by comparing to ground and satellite observations.

GVF and albedo are selected in the current study for three main reasons. First, accurate representation of GVF and albedo within meteorological models is critical for realistic simulation of local and regional meteorology over complex heterogeneous landscapes [Wetzel and Chang, 1988; Molders, 2001; Loridan et al., 2010; Vahmani and Hogue, 2014a]. Second, GVF and albedo are two physical characteristics of the land surface that get significantly altered via urbanization. In particular, loss of green vegetation in urban areas is one of the main contributors to the UHI. Third, the majority of UHI mitigation strategies involve urban vegetation and solar reflective cool roofs and pavements [Rosenfeld et al., 1995; Taha et al., 1999; Akbari et al., 2001; Taha, 2013]. These strategies modify GVF and/or albedo of urban surfaces, yet modeling efforts to predict the meteorological and climate impacts of these strategies often rely on predefined default model values and/or outdated climatological data to describe these surface physical characteristics for current time. Thus, realistic representation of these surface characteristics (i.e., albedo and GVF) in mesoscale modeling will lead to more accurate simulation of current urban climate and subsequently better estimates of expected changes induced by these strategies.

The second goal of this study is to investigate the role of land cover variability on determining the urban heat island within the Los Angeles region. Previous studies have reported that the nature of the UHI in Los Angeles is uniquely complex due to surrounding mountainous and coastal regions [Roth et al., 1989; Witw and LaDochy, 2008]. Furthering understanding of the UHI in Los Angeles necessitates adding to the current capabilities of WRF to account for high-resolution spatial variability in urban land surface characteristics and subsequent impacts on the surface energy balance and temperatures. In section 2, we describe the current default versions of WRF, the enhancements we made to address our research goals, and the simulations carried out. In sections 3.1–3.3, we report the differences between the current default versions of WRF versus our enhanced version. In section 3.4, we utilize the enhanced model to characterize the UHI in Los Angeles. To do so, we examine spatial and temporal variations in surface and air temperatures, and their relationships to urban surface characteristics including GVF, albedo, elevation, distance from ocean, and urban intensity. In this regard, this study not only sheds light on the complex relationships between temperatures and surface characteristics of Los Angeles but also sets the stage for further investigation on UHI mitigation strategies.

2. Methods and Data

2.1. WRF-UCM Model

In the current study, the WRF version 3.6.1 [Skamarock et al., 2008; Skamarock and Klemp, 2008] is used. WRF is a fully compressible, nonhydrostatic, mesoscale numerical weather prediction model that has been used for a variety of applications in urban environments (see Chen et al. [2011] for a review). WRF is coupled to the Noah land surface model (LSM), which includes an urban canopy model that allows for sophisticated representation of land-atmosphere coupling in urban areas. A description of the employed initial conditions, boundary conditions, spatial domain, and physics parameterizations is presented below.

In the current study, WRF is initialized and forced at its lateral boundaries with the North American Regional Reanalysis (NARR) data set [Mesinger et al., 2006]. All simulations are conducted from 6 July, 1900 UTC (12:00 P.M. local standard time) to 11 July 0700 UTC (12:00 A.M. local standard time), 2012, which represents an episode with clear skies and low wind speeds. The dominant winds in Los Angeles are onshore. For the selected timeframe, average wind speeds are 4.7 m s^{-1} at 2:00 P.M. and 1.4 m s^{-1} at 10:00 P.M. Air temperature variations are limited to a range of $19.3\text{--}34.9^\circ\text{C}$. The first 12 simulated hours are discarded as model spin-up. The simulations are performed over three (two-way) nested grids, centered over the Los Angeles metropolitan area, with horizontal grid resolutions of 18 km, 6 km, and 2 km, respectively (Figure 1). The largest domain (d01) covers most of the western U.S. and northern Mexico, the middle domain (d02) encompasses southern California, and the innermost domain (d03) covers the Los Angeles metropolitan area. The three domains have 71×99 , 91×103 , and 130×142 (east–west \times north–south) grid cells, respectively. Each domain uses 30 layers in the vertical.

The physical parameterization schemes used in the current study include the Monin-Obukhov scheme for the model surface layer, the Yonsei University (YSU) scheme [Hong et al., 2006] for the planetary boundary layer (PBL), the Kain-Fritsch cumulus scheme [Kain, 2004], the Lin scheme for microphysics [Lin et al., 1983], the Rapid Radiative Transfer Model [Mlawer et al., 1997] for longwave radiation, and the Dudhia scheme

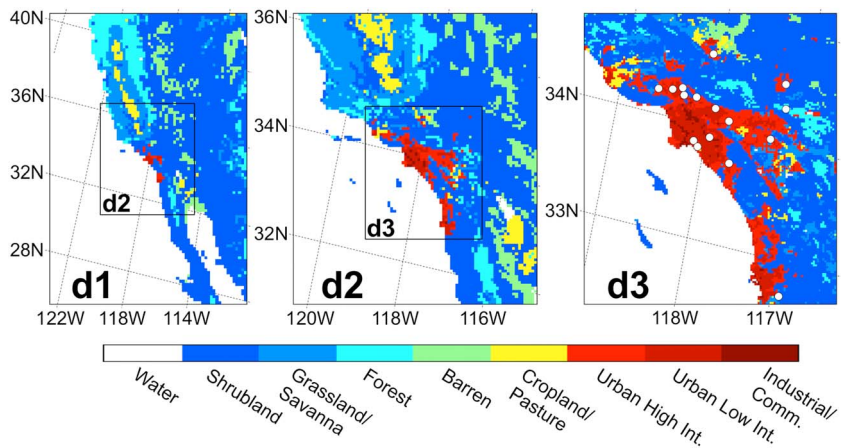


Figure 1. Geographical representation of the three nested WRF domains with 18, 6, and 2 km resolution for d1, d2, and d3, respectively. Land cover classifications are presented in each map. Over the innermost domain (d3), white circles are locations of the CIMIS and NCDC observation sites.

[Dudhia, 1989] for shortwave radiation. It should be noted that the cumulus parameterization is used only in domains 1 and 2. The atmosphere model is coupled to the Noah LSM [Chen and Dudhia, 2001] including the single-layer UCM [Kusaka and Kimura, 2004]. The UCM assumes infinitely long street canyons and takes into account the three-dimensional nature of urban surfaces including roof, wall, and road. This model also accounts for shadowing, reflections, and trapping of radiation in the urban canyon. Anthropogenic heat is not accounted for in our simulations. The UCM is employed for grid cells in which the dominant land cover type is one of three urban categories: low-intensity residential, high-intensity residential, and industrial/commercial, each of which has different assumed surface physical characteristics that by default are obtained from a predefined urban parameter table [Chen et al., 2011].

Land cover/land use is based on the National Land Cover Data (NLCD) for 2006, which has a spatial resolution of 30 m [Fry et al., 2011]. NLCD includes three urban types, which correspond to the three aforementioned urban categories in WRF/UCM. By default, the model assumes urban fractions of 50%, 90%, and 95% for low-intensity residential, high-intensity residential, and industrial/commercial, respectively. Instead of this default, we develop an independent impervious surface input data set based on the NLCD impervious surface data [Wickham et al., 2013], eliminating the need to assume fixed urban fraction values for each urban category. For each urban cell, this data set describes the fraction of the urban cell that is impervious (see section 2.3.1.2 for more details). Furthermore, we use the National Urban Database and Access Portal Tool (NUDAPT) [Ching et al., 2009] to define gridded and domain-specific urban morphological parameters including plan area fraction, mean building height, standard deviation of building height, area weighted mean building height, building surface to plan area ratio, and frontal area index.

Li and Bou-Zeid [2014] reported that estimation of surface temperatures in urban grid cells in the default version of Noah-UCM is flawed. The problem is related to the grid cell level turbulent transfer coefficient, which is inaccurately calculated using the momentum and thermal roughness lengths of the pervious portion of urban grid cells only. This leads to significant biases in simulated impervious surface temperatures calculated by the UCM. In the current study, the model code for computing land surface temperatures in urban cells was revised based on canyon temperature, roof surface temperature, and roof fraction [see *Li and Bou-Zeid, 2014*].

2.2. Study Domain and Ground-Based Observations

The focus of the current study is on the Los Angeles metropolitan region (Figure 1). The surrounding areas, as identified by the NLCD data set for 2006, include a variety of land cover types (e.g., water, barren land, forest, shrub land, and planted/cultivated land). The primary mountain ranges in the study domain are the Santa Monica and San Gabriel Mountains, located in the western and northern regions of the Los Angeles area, respectively. Farther away from the city, the eastern San Bernardino Mountains and southeastern San Jacinto Mountains are also captured in the current study domain. The valleys are generally the populated

and extensively developed areas, making Los Angeles the second largest metropolitan area in the United States, currently home to 13 million residents (U.S. Census Bureau, 2013, <http://www.census.gov/popest/data/metro/totals/2013/CBSA-EST2013-alldata.htm>). The city is one of the most highly urbanized and least green cities in the country [McPherson *et al.*, 2008].

We use hourly ground-based observations from 12 California Irrigation Management Information System (CIMIS) and 4 National Climatic Data Center (NCDC) stations to evaluate the simulations performed in this research. The location of each station is shown in Figure 1. The NCDC stations, which use Automated Surface Observing Systems (ASOS), are located at small airports within the Los Angeles metropolitan area in "large low-rise" climate zone, as defined by Stewart and Oke [2012]. These stations report hourly meteorological conditions at a standard reference height of 2 m. The regional CIMIS stations used in this study are mostly located in residential areas within "open low-rise" and "sparsely built" climate zone regions [Stewart and Oke, 2012]. CIMIS stations provide hourly weather data including 2 m air temperature. Using observed meteorological fields over a well-watered soil, hourly reference ET (ET_0) is also estimated for each site (<http://wwwcimis.water.ca.gov/cimis>). In the current study, ET_0 is converted to urban landscape ET employing an approach introduced by California Department of Water Resources [2000], and a landscape coefficient, which is calculated using vegetation species, density, and microclimate factors. Landscapes in the current study domain are assumed to have "moderate" water needs (average species factor = 0.50) and "average" density and microclimate factors (density and microclimate factors = 1). Based on these factors, a landscape coefficient of 0.50 (landscape coefficient = species factor × density factor × microclimate factor) is used to estimate the landscape ET values from the 12 CIMIS stations in the study area (Figure 1).

2.3. Satellite Observations

Satellite observations are retrieved from MODIS to produce high-resolution and domain-specific GVF and albedo inputs for WRF-UCM. MODIS images are acquired from the U.S. Geological Survey National Center for Earth Resource Observations and Science website available at <http://earthexplorer.usgs.gov>. The corresponding MODIS vegetation indices (MOD13A3) and reflectance (MCD43A4) products are gathered for the year 2012 and are used as reference data to compute spatially resolved monthly means of GVF and albedo, respectively. It should be noted that the accuracies of MODIS vegetation index and reflectance products are 0.025 and less than 5%, respectively [<http://landval.gsfc.nasa.gov>].

Satellite observations from MODIS are also used to derive land surface temperatures for evaluating the simulations. We utilize MOD11A1 and MYD11A1 (version 5, level 3) products that provide daily land surface temperatures at a spatial resolution of 1 km and overpass times of 11:00 A.M. and 10:00 P.M. local time.

The satellite observations used in the current study are regridded to the WRF coordinate system and resampled to the same spatial resolution (2 km). A quality control mask is also extracted and utilized to remove cloudy and low-quality pixels.

2.3.1. Green Vegetation Fraction

GVF is a key parameter within WRF and is defined as the fraction of the grid cell for which midday downward solar insolation is intercepted by a photosynthetically active green canopy. Thus, GVF acts as a weighting coefficient in partitioning total evaporation into direct evaporation from bare soil and canopy evapotranspiration [Chen and Dudhia, 2001]. In the Noah LSM, seasonal variation in GVF also defines seasonal variation in other surface physical characteristics, namely, albedo, LAI, emissivity, and roughness length. This is accomplished through a GVF-based factor, which is used to scale the parameter values within predefined ranges.

Despite the important role of GVF in land-atmosphere coupling in the model [Wetzel and Chang, 1988; Vahmani and Hogue, 2014a], WRF by default uses monthly varying five-year mean (1985–1990) green vegetation data observed by the advanced very high resolution radiometer (AVHRR) [Gutman and Ignatov, 1998]. This data set hereafter is referred to as AVHRR. It is noteworthy that the WRF version 3.6 also allows for using a relatively new global vegetation fraction data set based on MODIS climatological observations from 2001 to 2010, hereafter referred to as MODIS. In the current study, we replace these climatological GVF maps with high-resolution and real-time MODIS-based GVF maps, hereafter called Improved MODIS. In the next two sections, we present a detailed description of our implementation of satellite-based GVF in WRF-UCM.

2.3.1.1. Non-urban Grid Cells

In the current study, the monthly normalized difference vegetation index (NDVI) product (MOD13A3) acquired by MODIS is used to generate realistic and real-time monthly maps of GVF over the study domain. We use an approach introduced by *Gutman and Ignatov* [1998] which calculates GVF using equation (1),

$$GVF_{\text{pixel}} = \frac{NDVI - NDVI_0}{NDVI_\infty - NDVI_0} \quad (1)$$

where GVF_{pixel} is the pixel level GVF and $NDVI_0$ and $NDVI_\infty$ are constant NDVI values calculated using pixels with bare soil and dense vegetation in the current study domain, respectively. For non-urban areas, the estimated GVF values are directly incorporated to the Noah LSM framework within WRF. The implementation of GVF in urban grid cells is described in the next section.

2.3.1.2. Urban Grid Cells

As previously mentioned, urban grid cells in the WRF modeling framework are those whose dominant land use category is one of the three urban types: low-intensity residential, high-intensity residential, and industrial/commercial. Urban cells are divided into pervious and impervious parts using the aforementioned urban fraction parameter. The Noah LSM then simulates surface-atmosphere interactions for the pervious portion of the grid cell, and the UCM simulates those for the impervious portions.

The current default version of WRF-UCM uses predefined values for some land surface characteristics for the pervious part of urban grid cells. For example, albedo and emissivity are assumed to be 0.2 and 0.98, respectively. In addition, GVF values for the pervious part of urban grid cells correspond to that of the "natural" vegetation type, which translates to an unvarying GVF of 0.8 for all urban grid cells. In the current study, however, we modified the Noah-UCM code to use spatially varying GVF derived using satellite observations for both urban and non-urban grid cells.

Another complexity regarding GVF relates to different interpretations of GVF values as used by the model versus quantified by the observations. The Noah LSM, by default, defines GVF as the fraction of the pervious portion of the grid cell that is vegetated (i.e., pervious-level GVF). However, observed GVF data sets represent the fraction of the entire grid cell that is vegetated (i.e., pixel-level GVF). In order to correctly implement the real-time satellite observations in the model, we modify the model code to convert the observed pixel-level GVF to pervious-level GVF as described by equation (2),

$$GVF_{\text{pervious}} = \frac{GVF_{\text{pixel}}}{1 - f_{\text{urban}}} \quad (2)$$

where GVF_{pervious} and GVF_{pixel} are pervious- and pixel-level GVF, respectively, and f_{urban} represents the urban fraction of the pixel. Failure to modify GVF as described in equation (2) would result in significant underestimation of GVF for urban grid cells in the model.

2.3.2. Albedo

Albedo is a measure of the fraction of downwelling sunlight that is reflected. Surface albedo plays a dominant role in the dynamics of the surface energy balance [Dickinson, 1983; Dobos, 2003; Cedilnik *et al.*, 2012]. In the default WRF model, there are two ways of defining the surface albedo of non-urban grid cells. The first option utilizes a monthly climatological albedo data set based on AVHRR products from 1985 to 1991 [Csizar and Gutman, 1999]. This option is referred to as *AVHRR* hereafter. (In WRF, this option is known as "usemonalb.") The second option computes albedo using tabulated values that are dependent on the land cover type of the grid cell (hereafter called *Look-up table*). Note that the look-up table option also results in monthly varying albedos through a monthly varying GVF-based factor, which scales the albedo values within predefined ranges.

For urban grid cells in the default model, the albedo of the impervious portion is defined based on tabulated roof, wall, and road albedo values that are dependent on urban type. The default albedo of these three impervious surfaces is 0.2. The pervious portion of urban grid cells is by default assumed to also have an albedo of 0.2.

To overcome the shortcomings of the treatment of albedo in the default model, we use remotely sensed, MODIS-based albedo to generate heterogeneous, real-time monthly albedos, hereafter called *Improved MODIS*. The MODIS nadir BRDF-adjusted reflectance product (MCD43A4) is used in the current study. This product is corrected to represent local solar noon. View angle effects are also removed from the directional

Table 1. Summary of Simulations

Scenario	Source for GVF	Source for Albedo	Modified Model Code for GVF ^c	Modified Model Code for Albedo ^d
Default	AVHRR ^a	AVHRR ^a	-	-
MODIS_GVF	MODIS ^a	AVHRR ^a	-	-
Improved_GVF	Improved MODIS ^b	AVHRR ^a	X	-
Table_alb	AVHRR ^a	Look-up Table ^a	-	-
Improved_alb	AVHRR ^a	Improved MODIS ^b	-	X
Improved_GVF_alb	Improved MODIS ^b	Improved MODIS ^b	X	X

^aData sets are available for use with the standard WRF model.

^bData sets are developed in the current work.

^cTo maintain consistency with satellite observations, the modified code changes pixel-level GVF to pervious-level GVF for both urban and non-urban grid cells.

^dThe modified code incorporates satellite-observed albedo values for both pervious and impervious portions of urban grid cells, as well as non-urban grid cells.

reflectances resulting in stable and consistent background albedos. These albedos are directly implemented within the WRF model. We modified the model code to assign the measured pixel-level albedo to both pervious and impervious portions of each grid cell. Thus, relative to the default model, we improve the representation of albedo by using observed city-specific and spatially varying values for both urban and non-urban areas. It should be noted that the same remotely sensed albedo value is used for all the urban surfaces in a grid cell (i.e., road, wall, and roof).

2.4. Model Simulations

To investigate the changes in modeled urban meteorology induced by implementing the real-time satellite-based GVF and albedo data, we carry out a series of simulations as described in Table 1. The simulations investigate both default model configurations and implementations of new real-time MODIS-based data sets. The *Default* simulation uses AVHRR data sets for both GVF and albedo. *MODIS_GVF* and *Improved_GVF* cases incorporate different GVF data sets based on *MODIS* and *Improved MODIS*, respectively, while maintaining the same albedo maps as the *Default* case. Similarly, *Table_alb* and *Improved_alb* cases incorporate different albedo data sets based on *Look-up table* and *Improved MODIS*, respectively, while maintaining the default AVHRR GVF data. To understand how well the enhanced WRF performs in urban environments, the *Improved_GVF_alb* simulation utilizes real-time MODIS data (i.e., *Improved MODIS*) for both GVF and albedo. The three *Improved* simulations are conducted using the code modifications described in sections 2.3.1.2 and 2.3.2 to allow for accurate model interpretation of the newly developed data sets. The enhanced code correctly incorporates the pervious-level GVF instead of pixel-level values and introduces satellite-based and spatially varying albedo values to both pervious and impervious portions of urban grid cells. It should be noted that all the simulations use NLCD-based urban fraction and NUDAPT-based urban morphological parameters, explained in the section 2.1.

3. Results and Discussion

3.1. Default Versus Improved GVF and Albedo Data Sets

Figure 2 presents the real-time GVF data set developed in this research (*Improved MODIS*) as well as the two climatological data sets (AVHRR and MODIS) that are available for use in the standard WRF model. Difference maps are included in the supporting information (Figure S1). Note that Figure 2 presents pervious-level GVF, while pixel-level values are included in the supporting information (Figure S2).

Over urban regions, AVHRR and MODIS produce identical pervious-level GVFs in the model (Figures 2a and 2b). This is because by default the model assigns a GVF of 0.8 to the pervious portion of urban cells. Compared to our real-time *Improved MODIS* data set, this assumption leads to significant overestimation of GVF over most of the Los Angeles metropolitan area, particularly in the eastern portion of the domain. The MODIS data set produces inaccurate and unrealistic pixel-level GVF patterns over urban areas when compared to the *Improved MODIS* maps (see supporting information Figure S2b). Over non-urban grid cells, MODIS and *Improved MODIS* data sets produce similar patterns and show more spatial detail and variability compared to AVHRR. MODIS produces lower GVF values compared to the real-time *Improved MODIS* data (Figures 2b and 2c).

A comparison of seasonal variation in GVF from AVHRR, MODIS, and *Improved MODIS* is presented separately for urban and non-urban areas in Figure 2d. GVF values from *Improved MODIS* are lower (higher) than from

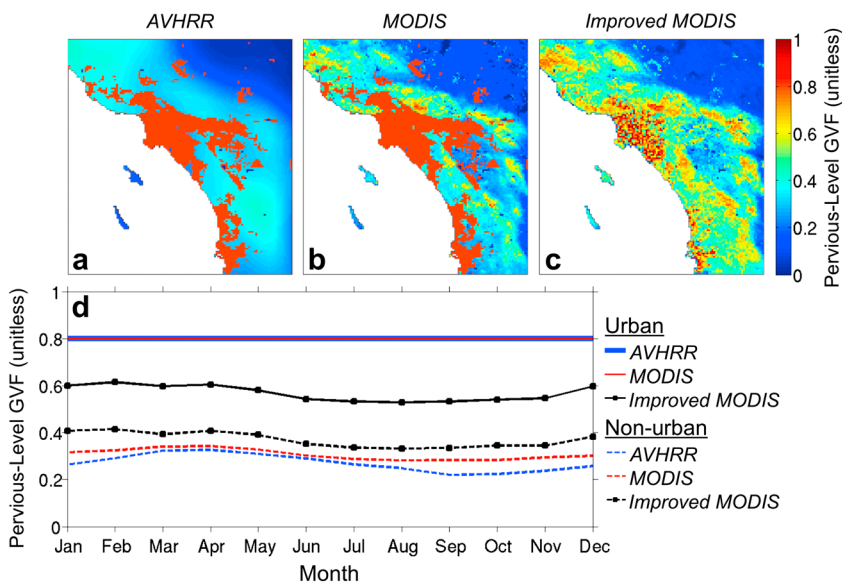


Figure 2. Spatial maps of GVF based on (a) climatology of AVHRR data, (b) climatology of MODIS data, and (c) real-time Improved MODIS data. All values shown are averaged over 2012. (d) Monthly time series of GVF averaged separately over urban and non-urban pixels are also shown. The two climatological data sets, AVHRR and MODIS, are available in the standard WRF model. The Improved MODIS data set is developed in this research. Note that values are pervious-level GVF, meaning that they represent the fraction of pervious area covered by green vegetation. Pixel-level GVF is shown in Figure S2.

AVHRR and MODIS over urban (non-urban) areas throughout the year. A subtle seasonal cycle in GVF is reported by all data sets over non-urban regions, while only Improved MODIS resolves the seasonal cycle over the urban grid cells (Figure 2d).

Albedo maps derived from Look-up table, AVHRR, and Improved MODIS are presented in Figure 3. Difference maps are included in the supporting information (Figure S3). Unlike the differences in GVF, which were more significant over urban parts of the domain, differences in albedo are more significant over the non-urban areas.

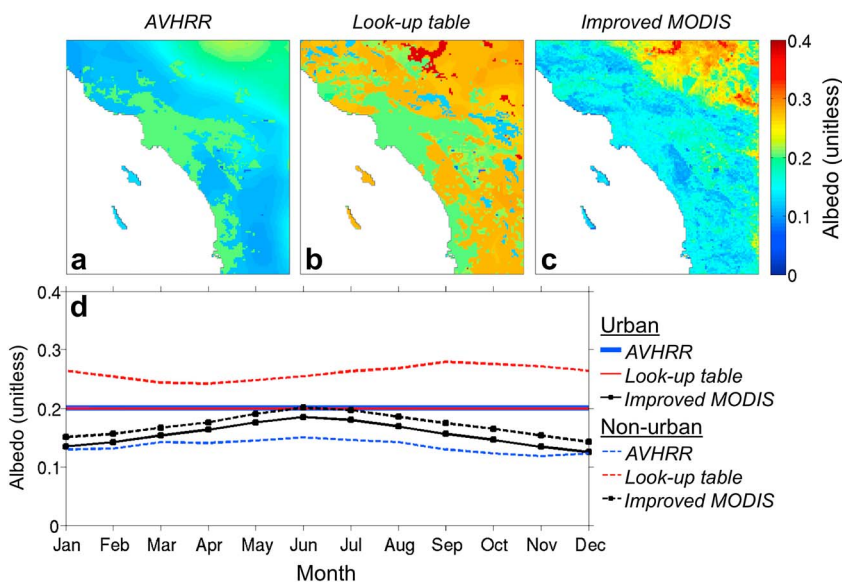


Figure 3. Spatial maps of albedo based on (a) climatology of AVHRR data, (b) Look-up table, and (c) real-time Improved MODIS data. All values are averaged over 2012. (d) Monthly time series of albedo averaged separately over urban and non-urban pixels are also shown. Data from AVHRR and Look-up table are available in the standard WRF model. The Improved MODIS data set is developed in this research.

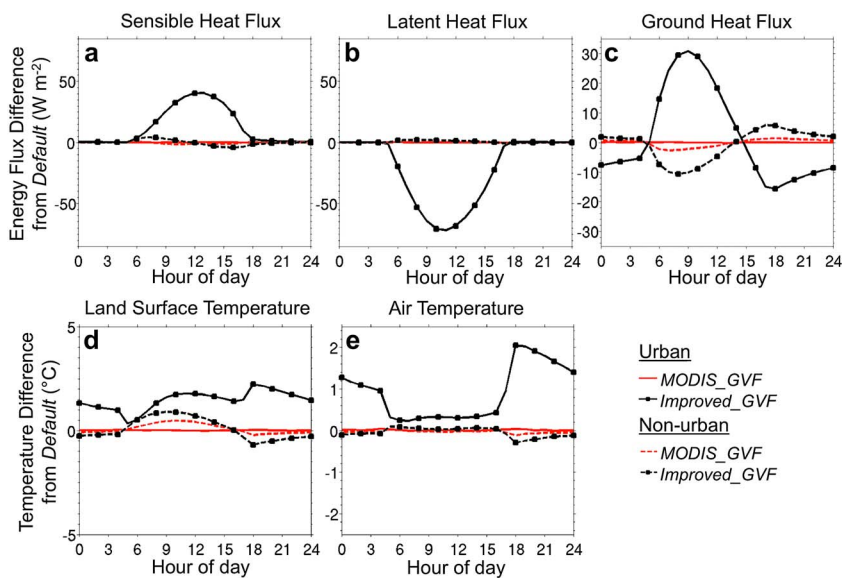


Figure 4. Simulated diurnal variations of the differences (relative to *Default*) for (a) sensible heat flux, (b) latent heat flux, (c) ground heat flux, (d) land surface temperature, and (e) 2 m air temperature. Results are presented for *MODIS_GVF* and *Improved_GVF* simulations. Values are averages over all urban and non-urban grid cells for 7–10 July 2012. Note that ground heat flux is positive downward.

When compared to *Improved MODIS*, non-urban albedo values are generally lower from *AVHRR* and higher from *Look-up table*. Over the urban areas, *AVHRR* and *Look-up table* produce uniform albedos of 0.2 (Figures 3a and 3b). This is due to the fact that the current version of WRF-UCM, by default, assumes an albedo of 0.2 for both pervious and impervious surfaces (i.e., roofs, roads, and walls) in urban grid cells. *Improved MODIS*, however, resolves the spatial variability in albedo within urban areas and results in overall lower albedo values (Figure 3c).

Figure 3d presents the annual cycle of monthly albedos from the three data sets. While differences among the data sets over non-urban areas are large throughout the year, differences over urban grid cells are large only during winter and small during summer.

3.2. Impact of Implementation of Satellite Observations on Simulated Temperatures and Surface Energy Balance

The influence of the different GVF and albedo inputs on the simulated surface energy balance and land surface and near-surface air temperatures is shown in Figures 4 to 7. The differences in spatial-mean diurnal profiles are shown separately for urban and non-urban grid cells (Figures 4 and 6). Absolute values are included in the supporting information (Figures S4 and S5). Spatial distributions are also presented for daytime (2 P.M.) and nighttime (10 P.M.) (Figures 5 and 7).

3.2.1. Green Vegetation Fraction

The *Default* and *MODIS_GVF* simulations produce almost identical sensible, latent, and ground heat fluxes over urban grid cells (Figure 4) since in each case the model uses the same simplifying assumption that assigns a GVF of 0.8 to these cells (see Figure 2). For *Improved_GVF*, however, relaxing the aforementioned assumption and instead including high-resolution spatial variability in satellite-based GVF (Figure 2) leads to changes in the surface energy balance of urban grid cells (Figure 4). During daytime, the *Improved_GVF* simulation produces substantially higher sensible heat fluxes and lower latent heat fluxes relative to the *Default* and *MODIS_GVF* cases (Figures 4a and 4b). This occurs due to decreases in GVF values over urban grid cells in *Improved MODIS* (Figure 2), leading to up to 68.3 W m^{-2} less energy being partitioned to latent heat (Figure 4b) and up to 40.5 W m^{-2} more energy being partitioned to sensible heat (Figure 4a). For *Improved_GVF*, simulated ground heat flux also shows significant changes over urban pixels, compared to the *Default* simulation (Figure 4c). These changes are induced by decreased green vegetation cover and include increases of up to 30.8 and 15.7 W m^{-2} in daytime downward and nighttime upward ground

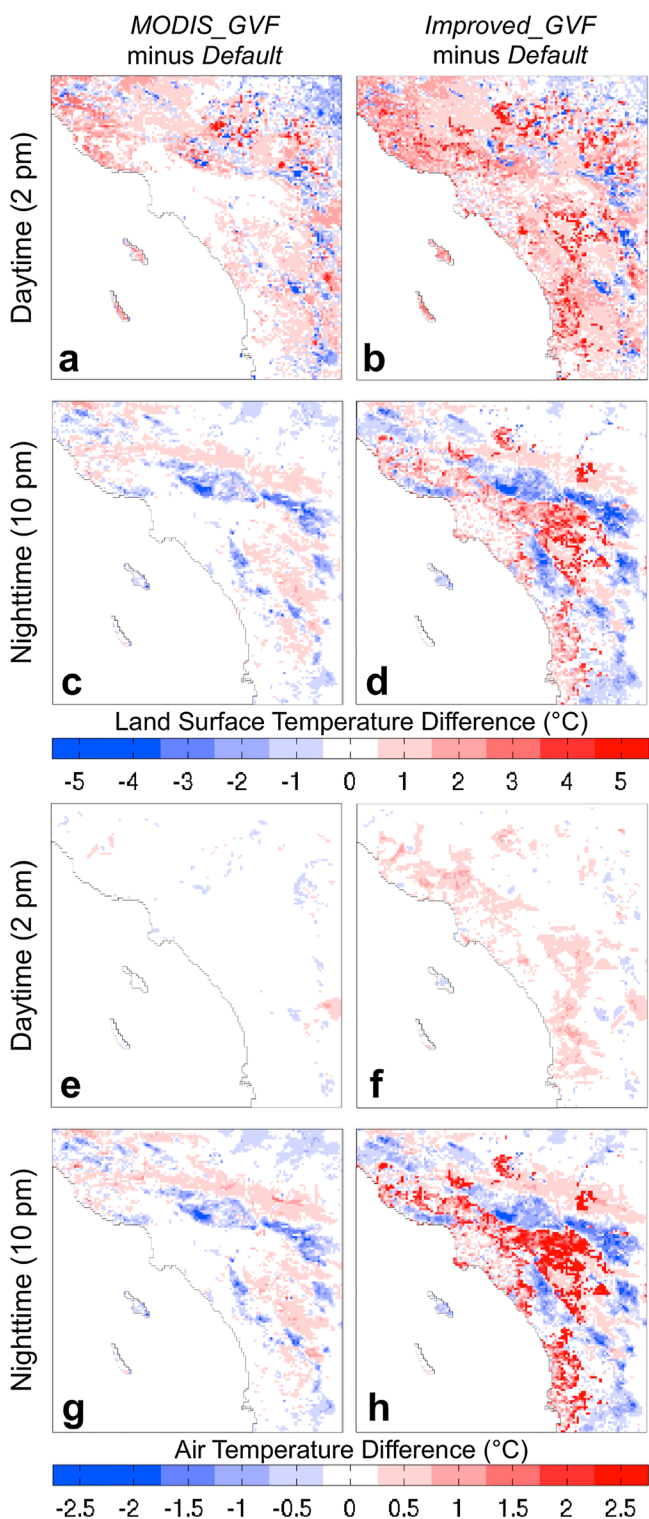


Figure 5. Simulated (a–d) land surface and (e–h) 2 m air temperature differences between *MODIS_GVF* and *Default* simulations (left column) and *Improved_GVF* and *Default* simulations (right column). Values are averaged for 7–10 July 2012.

heatfluxes, respectively. It should be noted that ground heat fluxes are positive downward. Regarding non-urban grid cells, the surface energy changes are less significant for both *Improved_GVF* and *MODIS_GVF*, a consequence of the fact that the GVF changes are less significant in these areas (Figure 2). However, decreases in daytime downward and nighttime upward ground heat fluxes are noticeable for *Improved_GVF* (Figure 4c). These changes are due to considerable GVF increases over some non-urban areas (Figure 2). Spatial maps of sensible, latent, and ground heat flux changes (included in the supporting information Figures S6 and S7) confirm higher sensible heat flux, lower latent heat flux, and higher nighttime (upward) ground heat fluxes over urban areas for the *Improved_GVF* case, compared to the *Default* case.

Changes in land surface and near-surface air temperatures relative to *Default* are dependent on time of day for the *MODIS_GVF* and *Improved_GVF* simulations (Figures 4d and 4e). The most significant changes are for urban grid cells in *Improved_GVF*, which uses real-time MODIS-based values for urban grid cells instead of the default model assumed GVF of 0.8. For the *Improved_GVF* case, the GVF-induced land surface and near-surface air temperature changes show similar diurnal behaviors with maximum temperature change of 2.3 and 2.2 $^{\circ}\text{C}$, respectively, occurring at 18:00 local time. Diurnal temperature changes reported here are due to shifts in the partitioning of surface energy between sensible and latent heat flux (Figures 4a and 4b). Nocturnal temperature changes are induced by increased upward ground heat flux at nighttime (Figure 4c). We hypothesize that these nocturnal effects are amplified due to vastly lower boundary layer heights during nighttime than during the day (see supporting information Figure S8).

Spatial temperature patterns from the *Default*, *MODIS_GVF*, and *Improved_GVF* simulations are presented

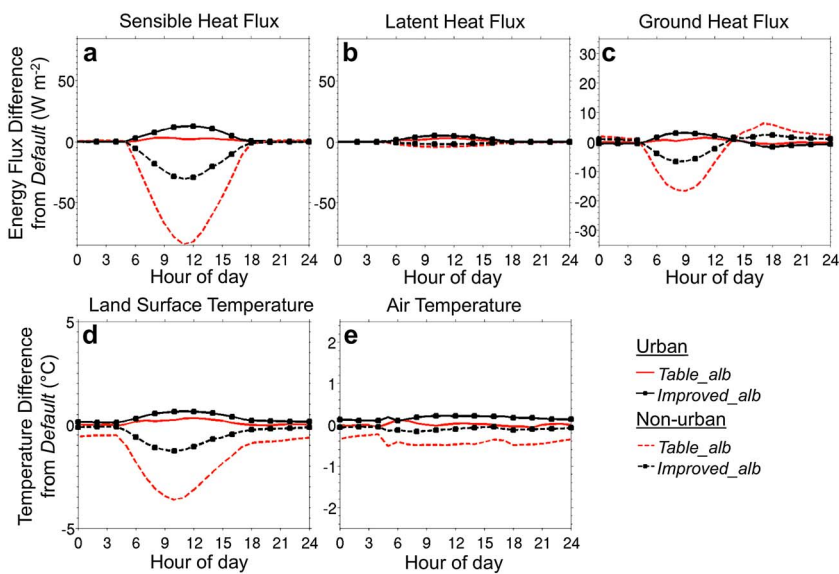


Figure 6. Simulated diurnal variations of the differences (relative to *Default*) for (a) sensible heat flux, (b) latent heat flux, (c) ground heat flux, (d) land surface temperature, and (e) 2 m air temperature. Results are presented for *Table_alb* and *Improved_alb* simulations. Values are averages over all urban and non-urban grid cells for 7–10 July 2012. Note that ground heat flux is positive downward.

in Figure 5. *Default* and *MODIS_GVF* produce nearly identical temperatures over urban grid cells due to the assumed GVF of 0.8 (see Figure 2). However, the *Improved_GVF* simulation shows higher land surface and near-surface air temperatures over urban areas relative to *Default* (Figures 5b, 5d, 5f, and 5h). This is a consequence of the lower urban GVFs in *Improved_GVF* versus the assumed value of 0.8 used in *Default*. The largest changes are observed during nighttime and over the eastern parts of the urban region where the GVF changes are most significant (Figure 2). Increases in nocturnal land surface and air temperatures for *Improved_GVF* versus *Default* are as large as 5.1 and 2.9°C, respectively (Figures 5d and 5h). Daytime changes in urban air temperatures for *Improved_GVF* versus *Default* range from 0.5 to 1.0°C.

Over non-urban areas, *MODIS_GVF* and *Improved_GVF* simulations result in similar spatial patterns of temperature change, with *Improved_GVF* minus *Default* showing larger values than *MODIS_GVF* minus *Default* (Figures 5). Lower nocturnal air and surface temperatures are simulated over the San Bernardino and San Gabriel Mountains, located immediately east and north of the Los Angeles area (Figures 5c, 5d, 5g and 5h). These temperature changes are induced by decreases in upward ground heat fluxes at nighttime (see supporting information Figures S7c and S7d). During daytime, differences in non-urban surface temperature are more complex and linked to indirect effects of changes in GVF on cloud cover and therefore downwelling shortwave radiation (see supporting information Figure S9).

3.2.2. Albedo

The changes in diurnal variations of surface energy budget terms as well as land surface and near-surface air temperatures are compared for the *Table_alb* and *Improved_alb* versus *Default* in Figure 6. *Default* and *Table_alb* produce nearly identical surface energy budget values for urban grid cells, a consequence of the fact that they both use the model *Default* assumption that urban grid cells have albedo of 0.2 (Figure 3). When compared to *Default*, the *Improved_alb* simulation results in small changes to the surface energy budget over urban areas (Figures 6a–6c). This is expected given that satellite-based albedo values over these regions during summer are similar to the *Default* model assumed value of 0.2 (see Figure 3). These subtle changes in the sensible, latent, and ground heat fluxes, which are limited to 12.9, 5.1, and 2.8 W m⁻², respectively, lead to mean increases in urban daytime surface and air temperature of 0.8 and 0.3°C, respectively, for *Improved_alb* minus *Default* (Figures 6d and 6e).

Over non-urban areas, albedo-induced changes are larger than over urban areas (Figure 6). Higher albedo values used in both *Table_alb* and *Improved_alb* simulations versus *Default* result in lower surface net radiations (of up to 122.8 and 44.5 W m⁻², respectively), leading to decreases in sensible heat fluxes (of up to 84.5 and 30.6 W m⁻², respectively) (Figure 6a). Corresponding changes in latent heat fluxes are minimal (Figure 6b).

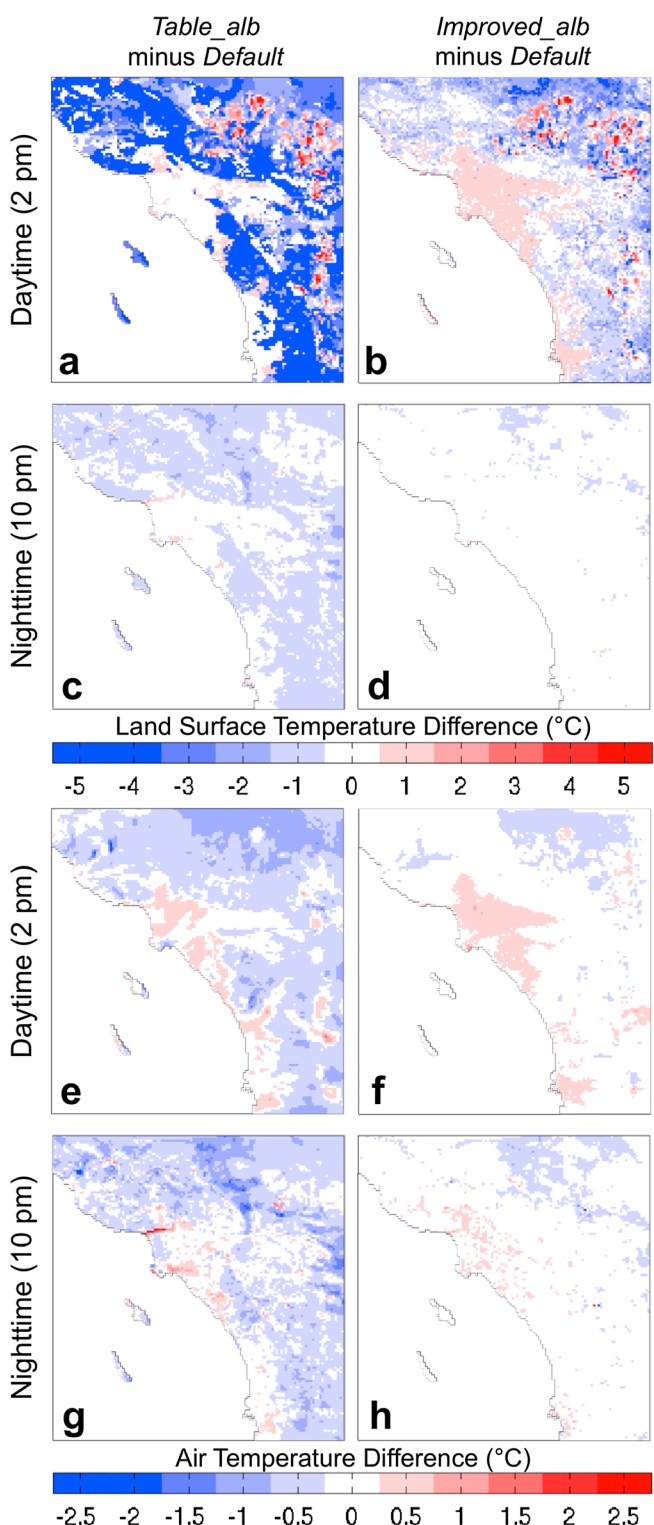


Figure 7. Simulated (a–d) land surface and (e–h) 2 m air temperature differences between *Table_alb* and *Default* simulations (left column), and *Improved_alb* and *Default* simulations (right column). Values are averaged for 7–10 July 2012.

This is an indicator of the high Bowen ratio in this region, resulting from low green vegetation coverage and dry soil over non-urban areas, which limits ET. An average daytime (7 A.M.–6 P.M.) Bowen ratio of 6.5 is calculated for non-urban areas. This is expected since summertime is a dry season in the Los Angeles region. Both *Table_alb* and *Improved_alb* simulations show lower land surface temperatures over non-urban areas relative to *Default*, with coolings of up to 3.7°C and 1.4°C, respectively. The larger temperature differences in *Table_alb* minus *Default* are consistent with the larger differences in albedo relative to *Improved_alb* versus *Default* (Figure 3). Air temperature changes are small and do not exceed 0.5°C (Figure 6e).

The spatial distributions of land surface and near-surface air temperature changes due to incorporation of look-up table (*Table_alb*) and MODIS (*Improved_alb*) based albedo maps are shown in Figure 7. Spatial maps of sensible, latent, and ground heat flux changes are included in the supporting information (Figures S10 and S11). For the majority of urban grid cells, lower albedo values in *Improved_alb* versus *Default* lead to higher sensible heat fluxes (see supporting information Figure S10b). This results in daytime warming of land surface and near-surface air by 1 and 0.5°C, respectively (Figures 7b and 7f). Over non-urban areas, higher albedo values lead to lower sensible heat fluxes (see supporting information Figure S10b). This results in daytime cooling of land surface temperatures in *Improved_alb* versus *Default* (Figure 7b). Nighttime albedo-induced land surface and air temperature changes are minimal for *Improved_GVF* minus *Default* (Figures 7d and 7h). Temperature changes over urban areas for *Table_alb* minus *Default* are also negligible (Figures 7a, 7c, 7e, and 7g). However, widespread and significant cooling effects are simulated over non-urban areas for *Table_alb* versus *Default* (Figures 7a, 7c, 7e, and 7g). This is a result of albedo-induced decreases in sensible heat fluxes (see supporting information

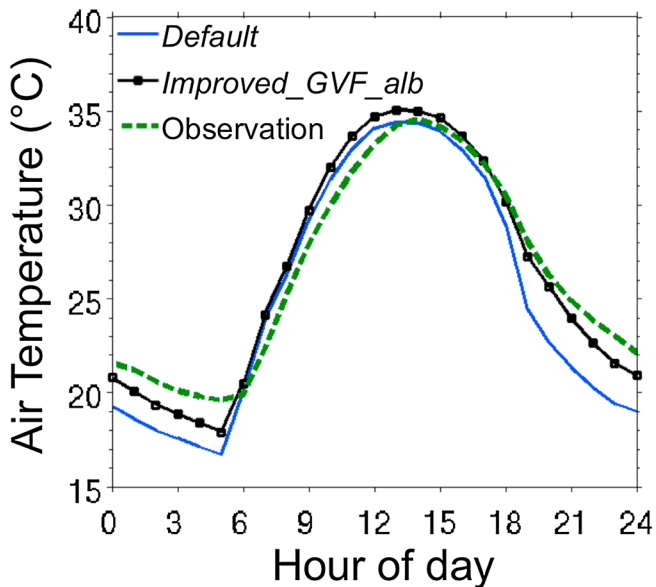


Figure 8. Diurnal variation in 2 m air temperature from ground observations, and the *Default* and *Improved_GVF_alb* simulations. The *Improved_GVF_alb* simulation adopts satellite-observed GVF and albedo data, whereas *Default* is the standard configuration of WRF-UCM. Values are averages over all urban and non-urban grid cells for 7–10 July 2012.

available potential energy (CAPE) in the atmosphere above the San Gabriel and San Bernardino mountains, which is subject to convective activity during summer.

3.3. Model Validation

We now compare simulations to ground and satellite observations to assess changes in the predictive capability of the model over the Los Angeles metropolitan area after implementing real-time satellite-derived GVF and albedo. As such, we evaluate two simulations: *Default*, and *Improved_GVF_alb*, which implements satellite-based GVF and albedo (Table 1). Observations used here include ground measurements of near-surface air temperature (Figures 8 and 9), ET (see supporting information Figures S12 and S13), as well as satellite-based land surface temperatures (Figure 10). (See sections 2.2 and 2.3 for more details on observations.)

Diurnal variation in 2 m air temperature from simulations and observations, averaged over 7–10 July 2012, is shown in Figure 8. Observations are from 16 CIMIS and NCDC stations over the Los Angeles metropolitan area. It is important to note that there is an inevitable inconsistency between ground-based observations, which generally represent a small footprint area of about 1 m^2 , and the modeled footprint area of corresponding 2 km grid cells. To help account for this fundamental disparity, observations from all stations are averaged and compared with the corresponding model-simulated averages from grid cells nearest to the station locations.

The *Default* simulation tends to underpredict 2 m air temperatures at night by 2 to 3°C (Figure 8). This is, in part, due to the overestimation of GVF and underestimation of albedo values in the default AVHRR-based data sets over urban areas (see Figures 2 and 3). For *Default*, the root-mean-square deviation (RMSD) for the simulation versus hourly observations is 2.3°C. Using more realistic MODIS-based GVF and albedo values, the *Improved_GVF_alb* simulation produces higher nocturnal 2 m air temperatures, which better match the observations (Figure 8). *Improved_GVF_alb* versus observations results in an RMSD of 1.2°C. The improved prediction of nocturnal air temperatures is consistent with that reported by Li *et al.* [2014] for the Pearl River Delta region of China. It is noteworthy that previous meteorological modeling studies have reported systematic shortcomings of boundary layer schemes including overestimations of nocturnal near-surface winds, which could contribute to the discussed underestimation of nighttime air temperature [e.g., Shimada *et al.*, 2011; Vautard *et al.*, 2012; Garcia-Menendez *et al.*, 2013; Zhang *et al.*, 2013].

Figure S10a). The most significant albedo-induced cooling is associated with daytime land surface temperature, which reaches 5.2°C over non-urban areas (Figure 7a). Nighttime land surface temperature changes, as well as daytime and nighttime air temperature changes, also show cooling patterns over non-urban areas with magnitudes up to 2.6, 2.1, and 2.3°C, respectively (Figures 7c, 7e, and 7g). There are scattered areas in the mountainous parts of the domain with increased daytime land surface temperatures (Figures 7a and 7b) in both *Table_alb* and *Improved_alb*, despite the albedo increase in these regions. The regions with surface temperature increases are associated with increased downwelling shortwave radiation (see supporting information Figure S12) stemming from decreased cloud cover. A likely explanation for the decreased cloud cover is that higher albedo reduces convective

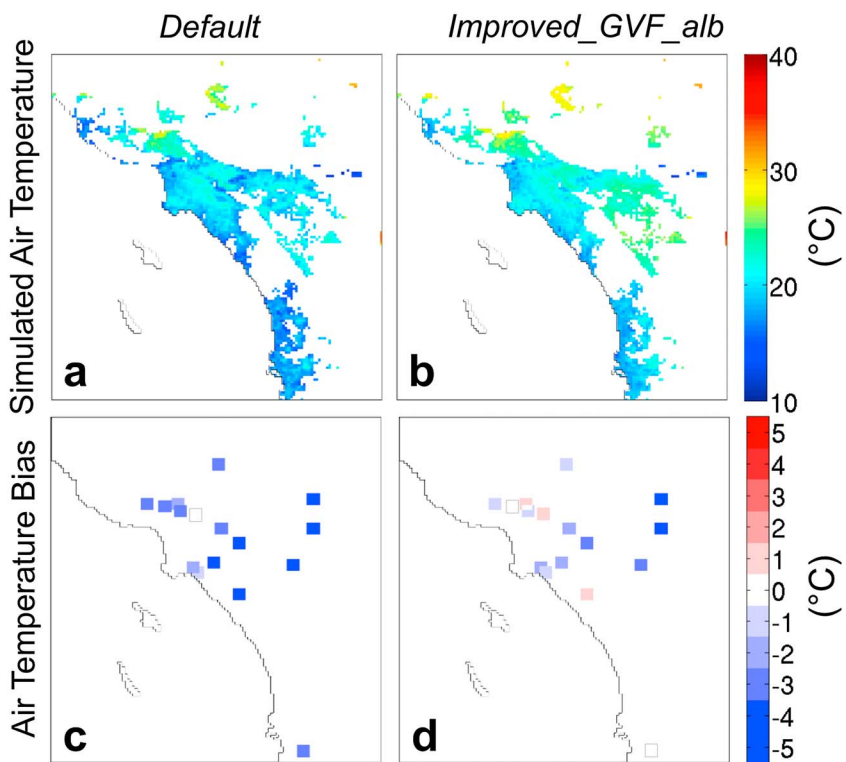


Figure 9. Spatial distribution of 2 m air temperature for *Default* and *Improved_GVF_alb* simulations (a, b), and air temperature biases (simulated – observed) using concurrent ground-based observations (c, d). Values are averaged over 7–10 July 2012 for 10 P.M. local time.

Figure 9 presents the simulated spatial distribution of 2 m air temperature for *Default* and *Improved_GVF_alb*, as well as comparisons to ground observations. Values shown are for 10 P.M. since previous studies have shown that the near-surface air temperature urban heat island is a nocturnal phenomenon especially in the period around and following sunset [Oke, 1982]. Comparisons of spatial variations in daytime

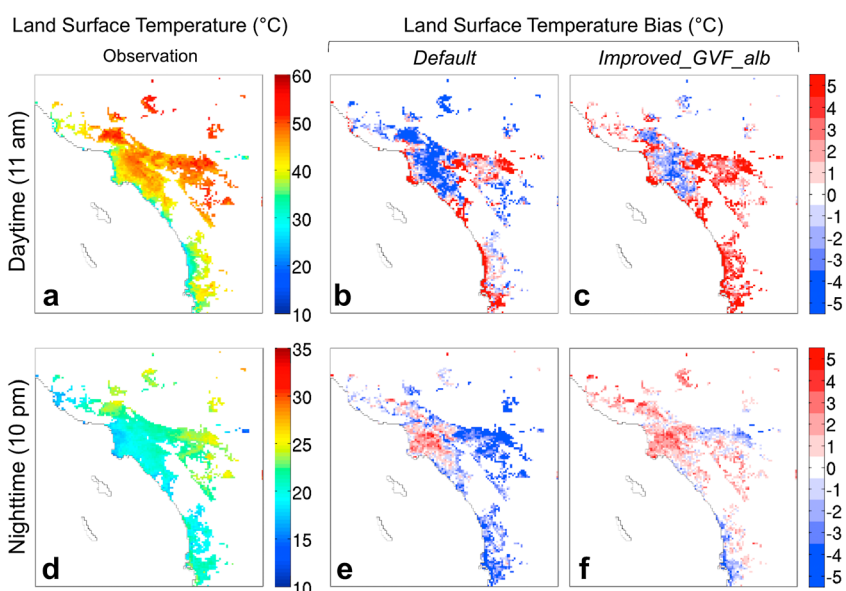


Figure 10. Spatial distribution of land surface temperature from MODIS daytime (11 A.M.) and nighttime (10 P.M.) observations (a, d), and land surface temperature biases (simulated – observed) for the *Default* and *Improved_GVF_alb* simulations (b, c, e, and f). Values are averaged over 7–10 July 2012.

air temperatures are included in the supporting information (Figure S13). Simulated versus observed nocturnal 2 m air temperatures at each measurement site shows marked improvements for *Improved_GVF_alb* versus *Default* (Figures 9c and 9d). For *Default*, 2 m air temperature is underestimated at almost all stations with a total RMSD of 3.8°C (Figure 9c). However, the implementation of MODIS-based GVF and albedo in *Improved_GVF_alb* reduces RMSD to 1.9°C (Figure 9d). Thus, accurately simulating nocturnal air temperature patterns depends significantly on realistic representation of GVF and albedo. The WRF prediction of daytime (at 2 P.M., local time) air temperatures, however, is not changed using MODIS-based GVF and albedo (RMSD of 1.0°C) (see supporting information Figure S13).

The model performance in producing ET temporal and spatial fluctuations is also evaluated using CIMIS-based ET observations. Our results show that *Improved_GVF_alb* produces lower ET rates compared to *Default*. This is due to decreased GVF in *Improved_GVF_alb* (see Figure 2). When evaluated against observations, both simulations show reasonable accuracy capturing ET variations (RMSD $\sim 0.08 \text{ mm h}^{-1}$ for both simulations). This analysis is included in the supporting information (Figures S14 and S15).

Maps of land surface temperatures from MODIS during day and night are shown in Figure 10. During daytime, satellite-based land surface temperatures are generally higher in inland locations (i.e., away from the Pacific Ocean) and over highly developed areas such as central Los Angeles, illustrating a strong daytime land surface temperature urban heat island effect (Figure 10a). During nighttime, the surface UHI pattern is not pronounced though inland temperatures remain generally warmer than near-coast regions (Figure 10d).

To further examine the improvements in model performance gained by implementing remotely sense GVF and albedo, simulated versus observed land surface temperatures are investigated (Figures 10b, 10c, 10e, and 10f). It is evident that the *Default* simulation underestimates daytime land surface temperatures over the central parts of Los Angeles (RMSD = 4.1°C) (Figure 10b). Implementing MODIS-based GVF and albedo in the *Improved_GVF_alb* case reduces the simulated cold biases over this region (Figure 10c). However, *Improved_GVF_alb* produces new regions of warm biases over the eastern and southern parts of the metropolitan area, leading to an RMSD that is nearly the same as that for *Default* (4.3°C). During nighttime, the *Default* simulation produces an RMSD of 2.6°C including large cold biases over the eastern and southern parts of the domain (Figure 10e). Biases are significantly reduced for *Improved_GVF_alb* (RMSD = 1.8°C), including improvements in the regions showing large cold biases in *Default* (Figure 10f). The improved model performance over these regions is largely associated with realistic estimation of GVF values (Figure 2). Nevertheless, over the central parts of the Los Angeles area, the land surface temperatures simulated by *Improved_GVF_alb* are still higher than MODIS observations (Figure 10f). We speculate that the overestimation of daytime and nighttime land surface temperature may be associated with the lack of urban irrigation in the current modeling framework. Previous studies over Los Angeles reported that irrigation-induced increases in latent heat flux can lead to land surface temperature decreases over urban areas [Vahmani and Hogue, 2014b].

It is noteworthy that an important source of uncertainty in meteorological models stems from insufficient understanding and simplified parameterization of physical processes, as well as coarse spatial resolution. Accuracy of physical process representations varies significantly from model to model and has been the topic of extensive past research [e.g., Penner et al., 2006; Fast et al., 2011; Shimada et al., 2011; Vautard et al., 2012; Yang et al., 2012; Garcia-Menendez et al., 2013; Zhao et al., 2013; Zhang et al., 2013].

3.4. Quantifying the UHI: Relationships Between Simulated Temperatures and Land Surface Characteristics

3.4.1. Relationships Using All Grid Cells

The accurate simulation of the diurnal cycle and spatial distribution of land surface and near-surface air temperatures (Figures 8–10 and section 3.2), as well as the realistic representation of GVF, albedo, and urban fraction, sets the stage for further investigation of the UHI in Los Angeles. Assessing the UHI in Los Angeles is difficult given that this region is surrounded by ocean and mountain ranges. Thus, spatial variations in temperatures are caused not only by land surface characteristics (e.g., urban fraction, albedo, and green vegetation fraction) but also by distance from the ocean and elevation. In an attempt to assess the factors that dictate the variations in surface and near-surface air temperature in the Los Angeles area, we evaluate relationships of grid cell level temperatures to distance from the ocean, elevation, urban fraction, GVF, and albedo (Figure 11). We note that while the surface temperature UHI has been investigated using

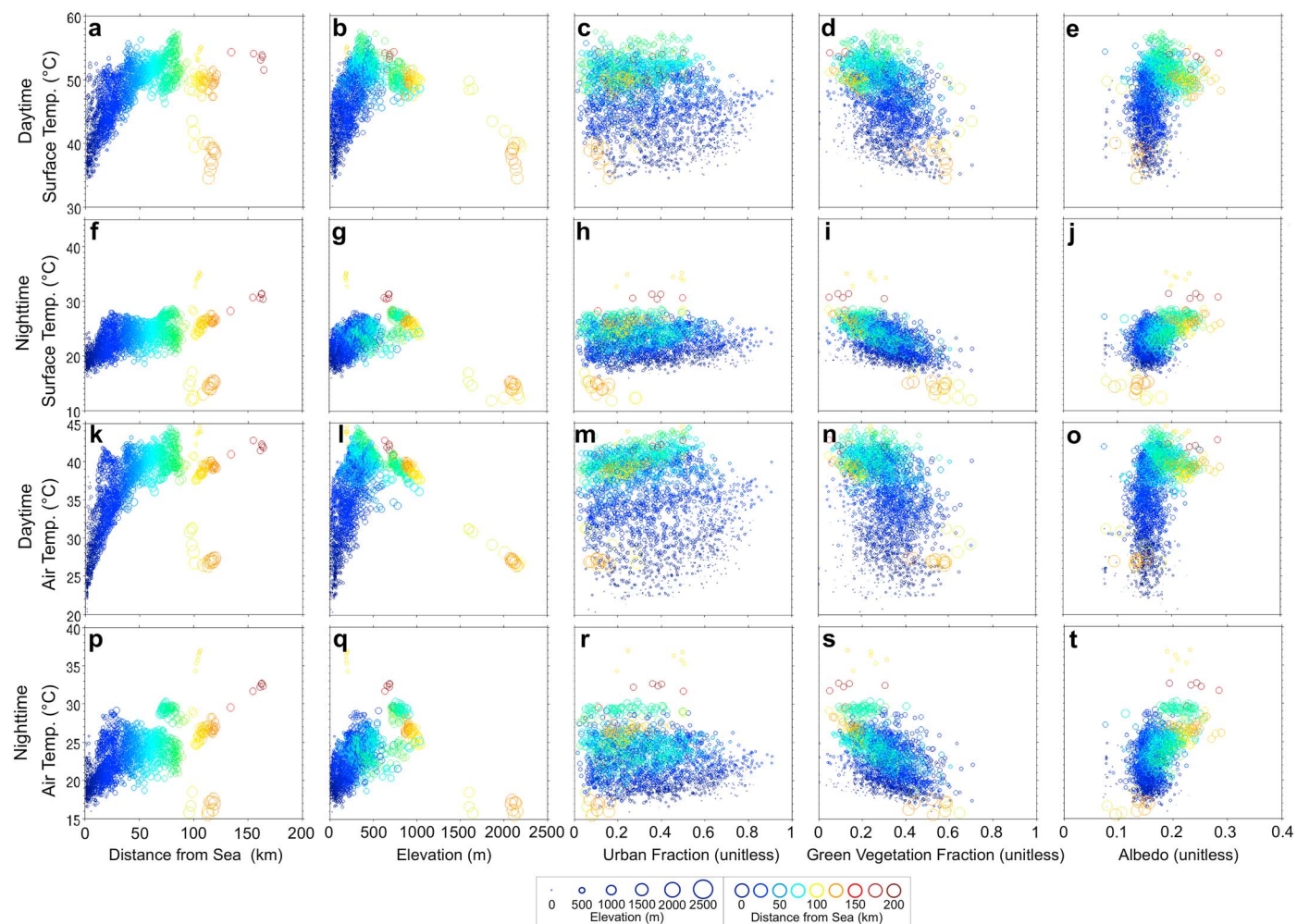


Figure 11. Relationships between simulated temperatures and (a, f, k, and p) distance from the sea, (b, g, l, and q) elevation, (c, h, m, and r) urban fraction, (d, i, h, and s) green vegetation fraction, and (e, j, o, and t) albedo. All values are from the *Improved_GVF_alb* simulation and use satellite-observed land surface characteristics. Values are shown for both daytime (2 P.M.) and nighttime (10 P.M.), and surface temperature and 2 m air temperature. Values are averaged over 7–10 July 2012 such that each point represents a different grid cell in the domain. Elevation and distance from the sea are indicated by the size and color of the circles, respectively.

satellite observations [Dousset and Gourmelon, 2003; Imhoff et al., 2010; Weng et al., 2014], measurements of surface air temperatures are spatially sparse, necessitating a model for investigation of the air temperature UHI.

Among the examined factors, distance from the ocean is the main contributor to variations in land surface and 2 m air temperatures, as illustrated in Figures 11a, 11f, 11k, and 11p. During daytime, the relationship between temperature and distance from the ocean is nonlinear. Daytime land surface and 2 m air temperatures show strong positive correlations to the distance from ocean over grid cells that are within about 50 km from the ocean. However, daytime temperatures become largely independent of distance from the ocean when farther than about 50 km.

Counterintuitively, positive correlations are seen between surface and 2 m air temperature versus elevation (Figures 11b, 11g, 11l, and 11q). This is due to the fact that in the Los Angeles metropolitan area, distance from the ocean and elevation are correlated. Inland areas are generally at higher elevations than coastal areas. The positive correlation between temperature and elevation holds only for elevation less than 600 m. At higher elevations (i.e., >600 m), the cooling effects of increased altitude start to surpass the warming effects of the increased distance from ocean. These patterns are consistent for daytime and nighttime surface and 2 m air temperatures. In general, the elevation-related cooling effects are most significant above 1500 m.

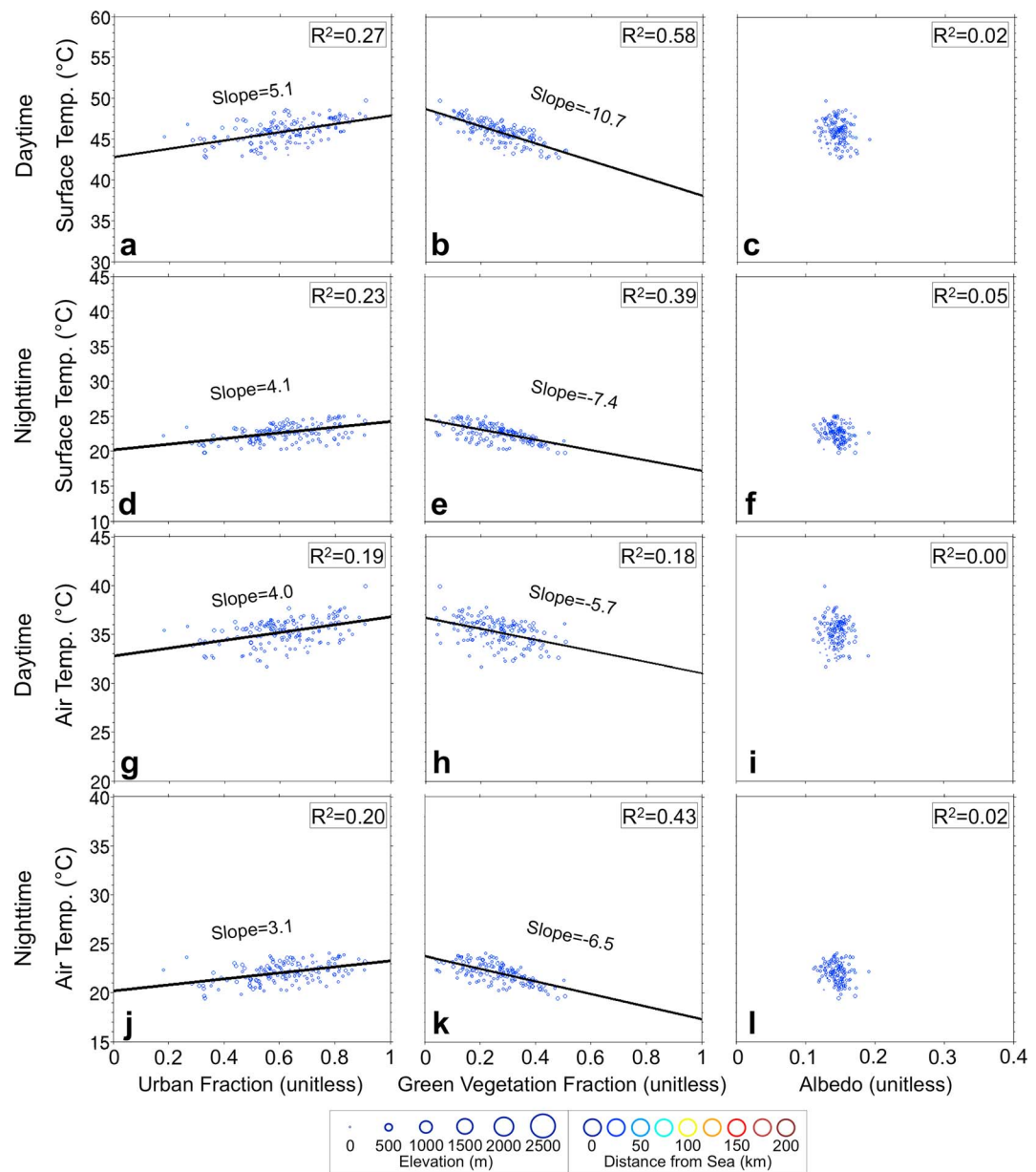


Figure 12. Relationships between simulated temperatures and (a, d, g, and j) urban fraction, (b, e, h, and k) green vegetation fraction, and (c, f, i, and l) albedo for conditionally sampled grid cells. Conditionally sampled grid cells limit variations in elevation to between 25 and 113 m above sea level, and distance from the sea to between 16 and 33 km. All values are from the *Improved_GVF_alb* simulation and use satellite-observed land surface characteristics. Values are shown for both daytime (2 P.M.) and nighttime (10 P.M.), and surface temperature and 2 m air temperature. Values are averaged over 7–10 July 2012 such that each point represents a different grid cell in the domain. Elevation and distance from the sea are indicated by the size and color of the circles, respectively. Black lines represent best fits using the least squares method, and coefficients of determination (R^2) are shown.

Remarkably, there are negligible correlations between surface and 2 m air temperatures versus urban fraction (Figures 11c, 11h, 11m, and 11r). Previous studies report significant correlations between land surface temperature and urban fraction in other cities [Yuan and Bauer, 2007; Imhoff et al., 2010; Zhou et al., 2014b]. The less pronounced relationships between temperature and urban fraction reported here is due to the uniquely strong influence of other factors including distance from the ocean and elevation in Los Angeles. Imhoff et al. [2010] assessed the relationship between land surface temperature and urban fraction for different impervious surface area zones in 38 cities within the continental United States. They reported an

average coefficient of determination of 80% for five cities in California (i.e., Fresno, Los Angeles, Sacramento, San Diego, and San Jose). They, however, did not specify a value for Los Angeles alone. Other studies acknowledged the complex nature of the UHI in Los Angeles due to surrounding mountainous and coastal regions [Roth *et al.*, 1989; Witiw and LaDochy, 2008].

Surface and near-surface temperatures are negatively correlated with GVF (Figures 11d, 11i, 11n, and 11s). The negative correlations are less significant during the day. Interestingly, correlations appear stronger for temperatures versus GVF than versus urban fraction.

Simulated surface and 2 m air temperatures show small and unexpectedly positive correlations with albedo (Figures 11e, 11j, 11o, 11t). One possible explanation for this is that urban areas that are farther from the ocean, in the eastern part of Los Angeles, tend to have up to 0.1 higher surface albedos in the current study domain (Figure 3c). Importantly, the relationships between temperatures and albedo should be interpreted with caution because of the very narrow range in albedos considered (Figure 11).

This analysis indicates that there is considerable complexity in the UHI in Los Angeles due to covariation in temperatures, distance from the ocean, elevation, urban fraction, albedo, and GVF.

3.4.2. Conditional Sampling

In an attempt to tease out the influence of land surface characteristics, namely, urban fraction, GVF, and albedo, on surface and 2 m air temperatures, we now conditionally sample grid cells based on distance from the ocean and elevation. The sampled grid cells are located at a distance from the ocean ranging from 16 to 33 km and have elevations from 25 to 113 m. Further attention is given to the biome of the analyzed grid cells, which are all located in the central region of the Los Angeles metropolitan area. In total, 167 grid cells are conditionally selected for this analysis (see supporting information for more information; Figure S16).

Relationships of daytime and nighttime temperatures versus urban fraction, GVF, and albedo for conditionally selected grid cells are assessed using the coefficients of determination (R^2) (Figure 12). In contrast with the previous section, which is focused in the entire metropolitan area, this analysis shows clear relationships between land surface and 2 m air temperatures versus urban fraction (Figures 12a, 12d, 12g, and 12j). Spatial variations in urban fraction contribute to 27, 23, 19, and 20% of the variance in daytime land surface temperature, nighttime land surface temperature, daytime 2 m air temperature, and nighttime 2 m air temperature, respectively.

Clearer relationships between temperatures and GVF are also detected (Figures 12b, 12e, 12h, and 12k). For the conditionally selected grid cells, spatial variations in GVF are responsible for 58, 39, 18, and 43% of the variance in daytime land surface temperature, nighttime land surface temperature, daytime 2 m air temperature, and nighttime air temperature, respectively. GVF influences are stronger for daytime land surface temperature than nighttime land surface temperature and for nighttime air temperature than daytime air temperature. This is important since surface and near-surface UHI intensities are greatest during the day and night, respectively [Roth *et al.*, 1989; Oke, 1982]. Based on these results, we hypothesize that strategies that include increasing GVF in urban areas can be effective in mitigating both the daytime surface and nighttime air temperature UHIs. This is consistent with previous studies that highlighted the key role of vegetation in attenuating the daytime surface temperature UHI [Zhou *et al.*, 2014a; Peng *et al.*, 2012; Dousset and Gourmelon, 2003] and the nighttime air temperature UHI [Yan *et al.*, 2014].

Simulated surface and air temperatures show negligible correlations to albedo (Figures 12c, 12f, 12i, and 12l). This is partially due to the small albedo variations in the studied region.

4. Summary

In the current study, we enhance a mesoscale meteorological model (WRF-UCM) by implementing high-resolution and real-time gridded MODIS-based observations to derive important land surface physical characteristics, including GVF and albedo. To enable the use of satellite-based GVF and albedo, the model code was also modified. We replace predefined unvarying values for the previous portion of urban grid cells with real-time, domain-specific, and spatially resolved MODIS-based data.

To investigate the improvements in modeled urban meteorology attained from implementing the real-time satellite-based GVF and albedo data, we carry out a series of simulations using both *Default* model

configurations and our real-time MODIS-based data sets. After implementing satellite-based surface characteristics within the modified model, the largest improvements are detected for nocturnal air temperatures. When compared with ground-based observations, simulated biases are reduced significantly (RMSD reduction from 3.8 to 1.9°C). This is critical since the near-surface air temperature UHI is mainly a nocturnal phenomenon. The model improvements in matching observed temperatures, compared to the default configuration, stem from a more accurate simulation of the surface energy balance, which depends on realistic representation of land surface characteristics, namely, GVF and albedo. Meanwhile, we acknowledge that an important source of uncertainty in meteorological models is associated with insufficient understanding and simplified parameterization of physical processes, as well as coarse spatial resolution, which are not the focus of the current study.

Taking advantage of our improved simulation of the diurnal cycle and spatial distribution of land surface and 2 m air temperatures, as well as our realistic representation of the land surface GVF, albedo, and urban fraction, we quantify relationships between these temperatures versus land surface physical characteristics (i.e., GVF, albedo, and urban fraction), as well as distance from the ocean and elevation, in the Los Angeles region. Distance from the ocean is found to be a main contributor to temperature variations. During the daytime, distance from the ocean most strongly influences temperatures in grid cells that are within about 50 km from the ocean. We also show that, as expected, elevations of 600 m and above are associated with significant cooling effects on surface and 2 m air temperatures. Thus, there is considerable complexity in the UHI for Los Angeles due to covariation in temperatures, distance from the ocean, elevation, urban fraction, albedo, and GVF. To tease out the influence of urban fraction, GVF, and albedo, on simulated temperatures, we conditionally sample grid cells based on distance from the ocean and elevation. After conditional sampling, considerable relationships between land surface and 2 m air temperatures versus urban fraction are detected. Urban fraction contributes to up to 27% of the variance in surface and 2 m air temperatures. Relationships between temperature fluctuations and GVF are most significant for daytime land surface temperature (coefficients of determination of up to 58%) and nighttime 2 m air temperature (coefficients of determination of up to 43%). Based on these results, we suggest that strategies that include increasing green vegetation in urban areas can be effective in mitigating both the daytime surface temperature and nighttime air temperature UHIs.

Acknowledgments

This research was supported by a fellowship from the Rose Hills Foundation and the USC Provost's Office. Computation for the work described in this paper was supported by the University of Southern California's Center for High-Performance Computing (hpc.usc.edu). We acknowledge the MODIS Science Team for processing and making publicly available the satellite data used in this study. Data from figures generated from WRF model output may be made available upon request from the corresponding author. MODIS observations are freely available from <http://earthexplorer.usgs.gov>.

References

- Akbari, H., M. Pomerantz, and H. Taha (2001), Cool surfaces and shade trees to reduce energy use and improve air quality in urban areas, *Solar Energy*, **70**, 295–310, doi:10.1016/S0038-092X(00)00089-X.
- Arnfield, A. J. (2003), Two decades of urban climate research: a review of turbulence, exchanges of energy and water, and the urban heat island, *Int. J. Climatol.*, **23**, 1–26, doi:10.1002/joc.859.
- Ban-Weiss, G. A., J. Woods, and R. Levinson (2015a), Using remote sensing to quantify albedo of roofs in California's seven largest cities. Part 1: Methods, *Solar Energy*, doi:10.1016/j.solener.2014.10.022.
- Ban-Weiss, G. A., J. Woods, D. Millstein, and R. Levinson (2015b), Using remote sensing to quantify albedo of roofs in California's seven largest cities. Part 2: Results and application to climate modeling, *Solar Energy*.
- California Department of Water Resources (2000), *A Guide to Estimating Irrigation Water Needs of Landscape Plantings in California: The Landscape Coefficient Method and WUCOLS III*, pp. 1–150, Dep. of Water Resour., State of Calif.
- Cedilnik, J., C. Dominique, J. F. Mahfouf, and J. L. Roujeau (2012), Impact assessment of daily satellite-derived surface albedo in a limited-area NWP model, *J. Appl. Meteorol. Climatol.*, **51**, 1835–1854, doi:10.1175/JAMC-D-11-0163.1.
- Chen, F., and J. Dudhia (2001), Coupling an advanced land surface-hydrology model with the Penn State-NCAR MM5 modeling system. Part I: Model implementation and sensitivity, *Mon. Weather Rev.*, **129**(4), 569–585, doi:10.1175/1520-0493(2001)129<0569:Calsh>2.0.CO;2.
- Chen, F., et al. (2011), The integrated WRF/urban modelling system: Development, evaluation, and applications to urban environmental problems, *Int. J. Climatol.*, **31**, 273–288, doi:10.1002/joc.2158.
- Cheng, F. Y., Y. C. Hsu, P. L. Lin, and T. H. Lin (2013), Investigation of the effects of different land use and land cover patterns on mesoscale meteorological simulations in the Taiwan area, *J. Appl. Meteorol. Climatol.*, **52**, 570–587, doi:10.1175/JAMC-D-12-0109.1.
- Cheng, Y. Y., and D. W. Byun (2008), Application of high resolution land use and land cover data for atmospheric modeling in the Houston-Galveston metropolitan area. Part I: Meteorological simulation results, *Atmos. Environ.*, **42**, 7795–7811, doi:10.1016/j.atmosenv.2008.04.055.
- Ching, J., et al. (2009), National Urban Database and Access Portal Tool, *Bull. Am. Meteorol. Soc.*, **90**, 1157–1168, doi:10.1175/2009BAMS2675.1.
- Crawford, T. M., D. J. Stensrud, F. Mora, J. W. Merchant, and P. J. Wetzel (2001), Value of incorporating satellite-derived land cover data in MMS/PLACE for simulating surface temperatures, *J. Hydrometeorol.*, **2**(5), 453–468, doi:10.1175/15257541(2001)002<0453:Voisdl>2.0.CO;2.
- Csiszar, I., and G. Gutman (1999), Mapping global land surface albedo from NOAA/AVHRR, *J. Geophys. Res.*, **104**, 6215–6228, doi:10.1029/1998JD200090.
- de Foy, B., L. T. Molina, and M. J. Molina (2006), Satellite-derived land surface parameters for mesoscale modelling of the Mexico City basin, *Atmos. Chem. Phys.*, **6**, 1315–1330.
- Dickinson, R. E. (1983), Land surface processes and climate-surface albedos and energy balance, *Adv. Geophys.*, **25**, 305–353, doi:10.1016/S0065-2687(08)60176-4.

- Dobos, E. (2003), *Albedo, Encyclopedia of Soil Science*, CRC Press, Chicago, doi:10.1201/NOE0849338304.ch15.
- Dousset, B., and F. Gourmelon (2003), Satellite multi-sensor data analysis of urban surface temperatures and landcover, *ISPRS J. Photogramm. Remote Sens.*, 58, 43–54, doi:10.1016/S0924-2716(03)00016-9.
- Dudhia, J. (1989), Numerical study of convection observed during the winter monsoon experiment using a mesoscale two-dimensional model, *J. Atmos. Sci.*, 46, 3077–3107, doi:10.1175/1520-0469(1989)046<3077:NSOCOD>2.0.CO;2.
- Fast, J. D., W. I. Gustafson Jr., E. G. Chapman, R. C. Easter, J. P. Rishel, R. A. Zaveri, G. A. Grell, and M. C. Barth (2011), The aerosol modeling testbed: A community tool to objectively evaluate aerosol process modules, *Bull. Am. Meteorol. Soc.*, 92, 343–360, doi:10.1175/2010BAMS2868.1.
- Fry, J., G. Xian, S. Jin, J. Dewitz, C. Homer, L. Yang, C. Barnes, N. Herold, and J. Wickham (2011), Completion of the 2006 National Land Cover Database for the conterminous United States, *Photogramm. Eng. Remote Sens.*, 77, 858–864.
- Garcia-Menendez, F., Y. Hu, and M. T. Odman (2013), Simulating smoke transport from wildland fires with a regional-scale air quality model: Sensitivity to uncertain wind fields, *J. Geophys. Res. Atmos.*, 118, 6493–6504, doi:10.1002/jgrd.50524.
- Grimmond, S. (2007), Urbanization and global environmental change: Local effects of urban warming, *Geogr. J.*, 173, 83–88, doi:10.1111/j.1475-4959.2007.232_3.x.
- Gutman, G., and A. Ignatov (1998), The derivation of the green vegetation fraction from NOAA/AVHRR data for use in numerical weather prediction models, *Int. J. Remote Sens.*, 19(8), 1533–1543, doi:10.1080/014311698215333.
- Hong, S.-Y., Y. Noh, and J. Dudhia (2006), A new vertical diffusion package with an explicit treatment of entrainment processes, *Mon. Weather Rev.*, 134, 2318–2341, doi:10.1175/MWR3199.1.
- Imhoff, M. L., P. Zhang, R. E. Wolfe, and L. Bouyoua (2010), Remote sensing of the urban heat island effect across biomes in the continental USA, *Remote Sens. Environ.*, 114(3), 504–513, doi:10.1016/j.rse.2009.10.008.
- Kain, J. S. (2004), The Kain–Fritsch convective parameterization: An update, *J. Appl. Meteorol.*, 43, 170–181, doi:10.1175/1520-0450(2004)043<0170:TKCPAU>2.0.CO;2.
- Kusaka, H., and F. Kimura (2004), Thermal effects of urban canyon structure on the nocturnal heat island: Numerical experiment using a mesoscale model coupled with an urban canopy model, *J. Appl. Meteorol.*, 43, 1899–1910, doi:10.1175/JAM2169.1.
- Lee, S.-H., and S.-U. Park (2008), A vegetated urban canopy model for meteorological and environmental modelling, *Boundary Layer Meteorol.*, 126, 73–102, doi:10.1007/s10546-007-9221-6.
- Li, D., and E. Bou-Zeid (2014), Quality and sensitivity of high-resolution numerical simulation of urban heat islands, *Environ. Res. Lett.*, 9, 055,001, doi:10.1088/1748-9326/9/5/055001.
- Li, M., Y. Song, X. Huang, J. Li, Y. Mao, T. Zhu, X. Cai, and B. Liu (2014), Improving mesoscale modeling using satellite-derived land surface parameters in the Pearl River Delta region, China, *J. Geophys. Res. Atmos.*, 119, 6325–6346, doi:10.1002/2014JD021871.
- Lin, Y.-L., R. D. Farley, and H. D. Orville (1983), Bulk parameterization of the snow field in a cloud model, *J. Climate Appl. Meteorol.*, 22, 1065–1092, doi:10.1175/1520-0450(1983)022<1065:BPOTSF>2.0.CO;2.
- Loridan, T., C. S. B. Grimmond, S. Grossman-Clarke, F. Chen, M. Tewari, K. Manning, A. Martilli, H. Kusaka, and M. Best (2010), Trade-offs and responsiveness of the single-layer urban parameterization in WRF: An offline evaluation using the MOSCEM optimization algorithm and field observations, *Q. J. R. Meteorol. Soc.*, 136, 997–1019, doi:10.1002/QJ.614.
- Loughner, C. P., D. J. Allen, D.-L. Zhang, K. E. Pickering, R. R. Dickerson, and L. Landry (2012), Roles of urban tree canopy and buildings in urban heat island effects: Parameterization and preliminary results, *J. Appl. Meteorol. Climatol.*, 51, 1775–1793, doi:10.1175/JAMC-D-11-0228.1.
- Manley, G. (1958), On the frequency of snowfall in metropolitan England, *Q. J. R. Meteorol. Soc.*, 84, 70–72, doi:10.1002/QJ.49708435910.
- McPherson, E. G., J. R. Simpson, Q. Xiao, and C. Wu (2008), Los Angeles 1-Million Tree Canopy Cover Assessment, (No. PSW-GTR-207), USDA Forest Service, Pacific Southwest Research Station, Albany, Calif.
- Meng, X. H., S. H. Lu, T. T. Zhang, J. X. Guo, Y. H. Gao, Y. Bao, L. J. Wen, S. Q. Luo, and Y. P. Liu (2009), Numerical simulations of the atmospheric and land conditions over the Jinta oasis in northwestern China with satellite-derived land surface parameters, *J. Geophys. Res.*, 114, D06114, doi:10.1029/2008JD010360.
- Mesinger, F., et al. (2006), North American Regional Reanalysis, *Bull. Am. Meteorol. Soc.*, 87, 343–360, doi:10.1175/BAMS-87-3-343.
- Mlawer, E. J., S. J. Taubman, P. D. Brown, M. J. Iacono, and S. A. Clough (1997), Radiative transfer for inhomogeneous atmospheres: RRTM, a validated correlated-k model for the longwave, *J. Geophys. Res.*, 102, 16,663–16,682, doi:10.1029/97JD00237.
- Molders, N. (2001), On the uncertainty in mesoscale modeling caused by surface parameters, *Meteorol. Atmos. Phys.*, 76(1–2), 119–141, doi:10.1007/s007030170043.
- Nichol, J., and W. S. Wong (2005), Modeling urban environmental quality in a tropical city, *Landscape Urban Plan.*, 73(1), 49–58, doi:10.1016/j.landurbplan.2004.08.004.
- Oke, T. R. (1976), The distinction between canopy and boundary-layer urban heat islands, *Atmosphere*, 14, 268–277, doi:10.1080/00046973.1976.9648422.
- Oke, T. R. (1982), The energetic basis of the urban heat-island, *Q. J. R. Meteorol. Soc.*, 108, 1–24, doi:10.1002/cj.49710845502.
- Owen, T. W., T. N. Carlson, and R. R. Gillies (1998), An assessment of satellite remotely-sensed land cover parameters in quantitatively describing the climatic effect of urbanization, *Int. J. Remote Sens.*, 19(9), 1663–1681, doi:10.1080/014311698215171.
- Peng, S. S., S. L. Piao, P. Ciais, P. Friedlingstein, C. Ottle, F. M. Breon, H. J. Nan, L. M. Zhou, and R. B. Myneni (2012), Surface urban heat island across 419 global big cities, *Environ. Sci. Technol.*, 46(2), 696–703, doi:10.1021/es2030438.
- Penner, J. E., J. Quaas, T. Storelvmo, T. Takemura, O. Boucher, H. Guo, A. Kirkevåg, J. E. Kristjánsson, and Ø. Seland (2006), Model intercomparison of indirect aerosol effects, *Atmos. Chem. Phys.*, 6, 3391–3405, doi:10.5194/acp-6-3391-2006.
- Rao, P. K. (1972), Remote sensing of “urban heat islands” from an environment satellite, *Bull. Am. Meteorol. Soc.*, 53, 647–648.
- Rosenfeld, A., H. Akbari, S. Bretz, B. Fishman, D. Kurn, D. Sailor, and H. Taha (1995), Mitigation of urban heat islands: Materials, utility programs, updates, *Energ. Build.*, 22, 255–265, doi:10.1016/0378-7788(95)00927-P.
- Roth, M., T. R. Oke, and W. J. Emery (1989), Satellite-derived urban heat islands from three coastal cities and the utilization of such data in urban climatology, *Int. J. Remote Sens.*, 10, 1699–1720, doi:10.1080/01431168908904002.
- Salamanca, F., A. Martilli, M. Tewari, and F. Chen (2011), A study of the urban boundary layer using different urban parameterizations and high-resolution urban canopy parameters with WRF, *J. Appl. Meteorol. Climatol.*, 50, 1107–1128, doi:10.1175/2010JAMC2538.1.
- Shimada, S., T. Ohsawa, S. Chikaoka, and K. Kozai (2011), Accuracy of the wind speed profile in the lower PBL as simulated by the WRF model, *Sola*, 7, 109–112, doi:10.2151/sola.2011-028.
- Skamarock, W. C., and J. B. Klemp (2008), A time-split nonhydrostatic atmospheric model for research and NWP applications, *J. Comput. Phys.*, 227, 3465–3485, doi:10.1016/j.jcp.2007.01.037.
- Skamarock, W. C., J. B. Klemp, J. Dudhia, D. O. Gill, D. M. Barker, M. G. Duda, X.-Y. Huang, W. Wang, and J. G. Powers (2008), A description of the advanced research WRF Version 3, NCAR Tech. Note NCAR/TN-475+STR, doi:10.5065/D68S4MVH.

- Stewart, I. D., and T. R. Oke (2012), Local climate zones for urban temperature studies, *Bull. Am. Meteorol. Soc.*, 93, 1879–1900, doi:10.1175/BAMS-D-11-00019.1.
- Susca, T., S. R. Gaffin, and G. R. Dell'Osso (2011), Positive effects of vegetation: Urban heat island and green roofs, *Environ. Pollut.*, 159, 2119–2126, doi:10.1016/j.envpol.2011.03.007.
- Taha, H. (2008a), Episodic performance and sensitivity of the urbanized MM5 (uMM5) to perturbations in surface properties in Houston Texas, *Bound. Layer Meteorol.*, 127, 193–218, doi:10.1007/s10546-007-9258-6.
- Taha, H. (2008b), Meso-urban meteorological and photochemical modeling of heat island mitigation, *Atmos. Environ.*, 42(38), 8795–8809, doi:10.1016/j.atmosenv.2008.06.036.
- Taha, H. (2013), The potential for air-temperature impact from large-scale deployment of solar photovoltaic arrays in urban areas, *Solar Energy*, 91, 358–367, doi:10.1016/j.solener.2012.09.014.
- Taha, H., S. Konopacki, and S. Gabersek (1999), Impacts of large-scale surface modifications on meteorological conditions and energy use: A 10-region modeling study, *Theor. Appl. Climatol.*, 62, 175–185, doi:10.1007/s007040050082.
- United Nations (2014), World Urbanization Prospects: The 2014 revision, Department of Economic and Social Affairs, Population Division, CD-ROM Edition, Data in digital form (United Nations publication, ST/ESA/SERA/361).
- Vahmani, P., and T. S. Hogue (2014a), High-resolution land surface modeling utilizing remote sensing parameters and the Noah UCM: A case study in the Los Angeles Basin, *Hydrol. Earth Syst. Sci.*, 18, 4791–4806, doi:10.5194/hess-18-4791-2014.
- Vahmani, P., and T. S. Hogue (2014b), Incorporating an urban irrigation module into the Noah Land Surface Model Coupled with an Urban Canopy Model, *J. Hydrometeorol.*, 15, 1440–1456, doi:10.1175/JHM-D-13-0121.1.
- Vautard, R., et al. (2012), Evaluation of the meteorological forcing used for the Air Quality Model Evaluation International Initiative (AQMEII) air quality simulations, *Atmos. Environ.*, 53, 15–37, doi:10.1016/j.atmosenv.2011.10.065.
- Voogt, J. A., and T. R. Oke (2003), Thermal remote sensing of urban climates, *Remote Sens. Environ.*, 86, 370–384, doi:10.1016/S0034-4257(03)00079-8.
- Weng, Q., P. Fu, and F. Gao (2014), Generating daily land surface temperature at Landsat resolution by fusing Landsat and MODIS data, *Remote Sens. Environ.*, 145, 55–67, doi:10.1016/j.rse.2014.02.003.
- Wetzel, P. J., and J. T. Chang (1988), Evapotranspiration from nonuniform surfaces: A 1st approach for short-term numerical weather prediction, *Mon. Weather Rev.*, 116(3), 600–621, doi:10.1175/1520-0493(1988)116<0600:Efnnsaf>2.0.Co;2.
- Wickham, J. D., S. V. Stehman, L. Gass, J. Dewitz, J. A. Fry, and T. G. Wade (2013), Accuracy assessment of NLCD 2006 land cover and impervious surface, *Remote Sens. Environ.*, 130, 294–304, doi:10.1016/j.rse.2012.12.001.
- Witiw, M. R., and S. LaDochy (2008), Trends in fog frequencies in the Los Angeles Basin, *Atmos. Res.*, 87(3), 293–300, doi:10.1016/j.atmosres.2007.11.010.
- Yan, H., S. Fan, C. Guo, J. Hu, and L. Dong (2014), Quantifying the impact of land cover composition on intra-urban air temperature variations at a mid-latitude city, *PLoS One* 9(7), e102124, doi:10.1371/journal.pone.0102124.
- Yang, B., Y. Qian, G. Lin, R. Leung, and Y. Zhang (2012), Some issues in uncertainty quantification and parameter tuning: A case study of convective parameterization scheme in the WRF regional climate model, *Atmos. Chem. Phys.*, 12, 2409–2427, doi:10.5194/acp-12-2409-2012.
- Yuan, F., and M. E. Bauer (2007), Comparison of impervious surface area and normalized difference vegetation index as indicators of surface urban heat island effects in Landsat imagery, *Remote Sens. Environ.*, 106(3), 375–386, doi:10.1016/j.rse.2006.09.003.
- Zhang, H., Z. Pu, and X. Zhang (2013), Examination of errors in near-surface temperature and wind from WRF numerical simulations in regions of complex terrain, *Weather Forecasting*, 28(3), 893–914, doi:10.1175/Waf-D-12-00109.1.
- Zhao, C., et al. (2013), A sensitivity study of radiative fluxes at the top of atmosphere to cloud-microphysics and aerosol parameters in the community atmosphere model CAM5, *Atmos. Chem. Phys.*, 13, 10,969–10,987, doi:10.5194/acp13-10969-2013.
- Zhao, L., X. Lee, R. B. Smith, and K. Oleson (2014), Strong contributions of local background climate to urban heat islands, *Nature*, 511(7508), 216–219, doi:10.1038/nature13462.
- Zhou, D. C., S. Q. Zhao, S. G. Liu, L. X. Zhang, and C. Zhu (2014a), Surface urban heat island in China's 32 major cities: Spatial pattern and drivers, *Remote Sens. Environ.*, 152, 51–61, doi:10.1016/j.rse.2014.05.017.
- Zhou, W., Y. Qian, X. Li, W. Li, and L. Han (2014b), Relationships between land cover and the surface urban heat island: Seasonal variability and effects of spatial and thematic resolution of land cover data on predicting land surface temperatures, *Landscape Ecol.*, 29, 153–167, doi:10.1007/s10980-013-9950-5.